nature physics

ARTICLES

PUBLISHED ONLINE: 22 MAY 2011 | DOI: 10.1038/NPHYS2006

Electron-spin excitation coupling in an electron-doped copper oxide superconductor

Jun Zhao[1†‡], F. C. Niestemski[2†‡], Shankar Kunwar[2‡], Shiliang Li[1,3], P. Steffens[4], A. Hiess[4], H. J. Kang[5], Stephen D. Wilson[2], Ziqiang Wang[2], Pengcheng Dai[1,3,6]* and V. Madhavan[2]*

High-temperature (high-T_c) superconductivity in the copper oxides arises from electron or hole doping of their antiferromagnetic (AF) insulating parent compounds. The evolution of the AF phase with doping and its spatial coexistence with superconductivity are governed by the nature of charge and spin correlations, which provides clues to the mechanism of high-T_c superconductivity. Here we use neutron scattering and scanning tunnelling spectroscopy (STS) to study the evolution of the bosonic excitations in electron-doped superconductor $Pr_{0.88}LaCe_{0.12}CuO_{4-\delta}$ with different transition temperatures (T_c) obtained through the oxygen annealing process. We find that spin excitations detected by neutron scattering have two distinct modes that evolve with T_c in a remarkably similar fashion to the low-energy electron tunnelling modes detected by STS. These results demonstrate that antiferromagnetism and superconductivity compete locally and coexist spatially on nanometre length scales, and the dominant electron–boson coupling at low energies originates from the electron-spin excitations.

High-T_c superconductivity in the copper oxides arises from either electron or hole doping of their antiferromagnetic parent compounds[1,2]. There is experimental and theoretical evidence suggesting that antiferromagnetism is a competing phase to superconductivity in both electron- and hole-doped materials[1–5]. In samples where antiferromagnetism and superconductivity coexist, the spatial configuration of these two phases can provide important information on the strength of electron correlations[3,5] and the extent to which antiferromagnetism contributes to electron pairing[1–5]. Electron correlations in the hole- and electron-doped materials can be quite different[5]. Whereas doped electrons reside in the Cu 3d orbitals with correlations involving primarily d-electrons[2], doped holes form Zhang–Rice singlets moving in the background of Cu spins[1] and are subject to stronger correlations[1–7]. The electron-doped materials are uniquely suited to studying the competition between antiferromagnetic (AF) and superconducting orders. In hole-doped copper oxides, such as $La_{2-x}Ba_xCuO_4$ near $x = 1/8$, strong electron correlation effects force the doped charge carriers into metallic rivers or stripes that are distributed as inhomogeneous patterns inside the AF insulating background[6,7]. Here, hole doping of the parent compound La_2CuO_4 is achieved by replacing the trivalent La^{3+} with the divalent Ba^{2+}, which also induces chemical disorder and affects the lattice properties[6–8], thus making it difficult to disentangle disorder from the effect of hole doping. Unlike their hole-doped counterparts, electron doping is carried out by replacing the $(Pr, La)^{3+}$ in the parent compound $(Pr, La)_2CuO_4$ with the Ce^{4+} to form a non-superconducting antiferromagnet $Pr_{1-x}LaCe_xCuO_4$ (refs 2,9). Further post-growth annealing treatment is required to suppress the static AF order and obtain superconductivity[2]. As the annealing process only removes a tiny amount of excess oxygen and has minimal effects on its lattice structure[2,8,10,11], electron-doped materials provides an unique platform to study the evolution from AF order to superconductivity through the oxygen annealing process[10–15].

In the electron-doped materials, there are bulk signatures of coexisting AF and superconducting phases[2,9,16,17]. These measurements, however, cannot distinguish nanoscale spatial coexistence from larger scale phase segregation. Here we report advances made by combined neutron scattering and scanning tunnelling spectroscopy (STS) studies on nominally identical electron-doped superconducting $Pr_{0.88}LaCe_{0.12}CuO_{4-\delta}$(PLCCO) samples with different T_c obtained through the oxygen annealing process[10,11]. The $T_c = 24$ K PLCCO system is a pure superconductor, whereas the $T_c = 21$ K sample has static AF order coexisting with superconductivity[10–15]. Using polarized and unpolarized neutron triple-axis spectroscopy (see Supplementary Information), we show that spin excitations in the $T_c = 24$ K PLCCO have two modes near 2 and 10.5 meV (ref. 14). On annealing to obtain the $T_c = 21$ K PLCCO system, the intensity of the 2 meV mode increases dramatically, whereas the 10.5 meV mode is downshifted to 9.5 meV and becomes much weaker across T_c (refs 11,14). Remarkably, our STS measurements on the same samples also reveal two modes that evolve with T_c in an almost identical manner. A comparison of the spatial and temperature dependence of the neutron and STS modes suggests that the 2 meV mode is associated with antiferromagnetism whereas the ∼10 meV mode is connected with superconductivity. As the oxygen annealing process that changes T_c from 21 to 24 K in PLCCO is not expected to affect lattice (phonon) properties[2,8,10,11], our data indicate that spin excitations are indeed observed in STS data and the dominant electron–boson coupling at low energies originates from the electron-spin excitations[18] rather than electron–phonon

[1]Department of Physics and Astronomy, The University of Tennessee, Knoxville, Tennessee 37996-1200, USA, [2]Department of Physics, Boston College, Chestnut Hill, Massachusetts 02467, USA, [3]Beijing National Laboratory for Condensed Matter Physics, Institute of Physics, Chinese Academy of Sciences, Beijing 100080, China, [4]Institut Laue Langevin, 6 Rue Jules Horowitz BP 156, F-38042 Grenoble Cedex 9, France, [5]NIST Center for Neutron Research, National Institute of Standards and Technology, Gaithersburg, Maryland 20899-8562, USA, [6]Neutron Scattering Science Division, Oak Ridge National Laboratory, Oak Ridge, Tennessee 37831, USA. †These authors contributed equally to this work. ‡Present addresses: Department of Physics, University of California, Berkeley, California 94720-7300, USA (J.Z.); Department of Physics, Stanford University, Stanford, California 94305, USA (F.C.N.); Department of Physics, King Fahd University of Petroleum and Minerals, Dhahran, 31261, Saudi Arabia (S.K.). *e-mail: pdai@utk.edu; madhavan@bc.edu.

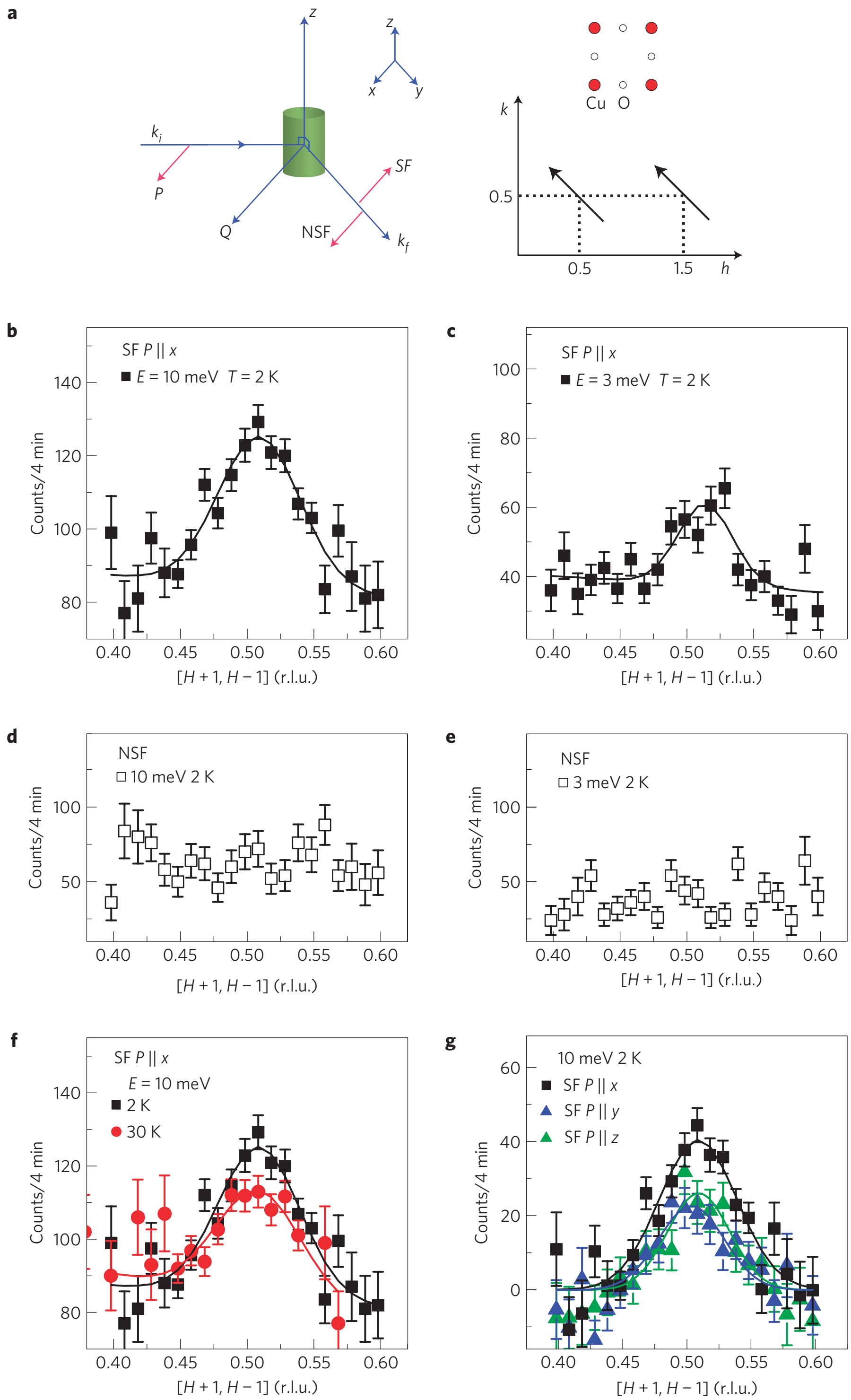

Figure 1 | Schematic diagram of polarized neutron scattering set-up and polarized neutron scattering data at various temperatures. a, Real and reciprocal space of the CuO_2 plane. The position in reciprocal space at wave vector $\mathbf{Q}=(q_x,q_y,q_z)$ Å^{-1} is labelled as $(H,K,L)=(q_xa/2\pi, q_yb/2\pi, q_zc/2\pi)$ reciprocal lattice units (r.l.u.), where the tetragonal unit cell of PLCCO (space group I_4/mmm) has lattice parameters of $a=b=3.98$ Å, $c=12.27$ Å. Our polarized neutron scattering experiments were carried out on the IN20 thermal neutron three-axis spectrometer at Institut Laue Langevin with a fixed final neutron energy of $E_f=14.7$ meV. With the Cryopad set-up, we can study the magnetic excitations of PLCCO in a strictly zero magnetic field (<10 mG), thus avoiding errors due to flux inclusion or field expulsion in the superconducting phase of the sample. Left panel: schematic diagram of polarized neutron scattering set-up. Red arrows indicate the neutron spin polarization directions P. k_i and k_f are incident and scattered neutron momentum, respectively. Right panel: real and reciprocal space of the CuO_2 plane. **b** and **d**, **Q**-scans through ($\mathbf{Q}=(1.5,-0.5,0)$) at $E=10$ meV and 2 K in the SF and NSF channels, respectively. **c** and **e**, The same **Q**-scans at $E=3$ meV and 2 K in the SF and NSF channels, respectively. **f**, Temperature dependence of the SF scattering at $E=10$ meV. **g**, Neutron spin polarization dependence of the resonance at $E=10$ meV. The solid lines are Gaussian fits on linear backgrounds. The error bars indicate one standard deviation throughout the paper.

interactions[19]. If high-T_c superconductivity in copper oxides requires a bosonic 'pairing glue'[20–22], these results would suggest that spin excitations are the mediating glue for the electron pairing and superconductivity in PLCCO.

In previous unpolarized neutron scattering experiments on the $T_c = 24$ K PLCCO, a resonance mode centred at the AF wave vector $\mathbf{Q} = (1/2, 1/2)$ was observed near 10.5 meV (ref. 14). To confirm the magnetic nature of the resonance, we carried out neutron polarization analysis on the $T_c = 24$ K sample (Fig. 1a). For neutron polarizations along the **Q**-direction, magnetic scattering flips the polarization direction of the incident neutrons (neutron spin-flip or SF) whereas neutron non-spin-flip (NSF) scattering probes pure nuclear scattering[23]. The neutron polarization analysis can therefore unambiguously separate magnetic scattering from nonmagnetic scattering processes[23]. Similar **Q**-scans were obtained for both the SF and NSF scattering at 2 K, with energy transfers near the resonance ($E = 10$ meV) and well below it ($E = 3$ meV) (Fig. 1b–e). Whereas a peak centred at the AF ordering wave vector is observed for the SF channel (Fig. 1b,c), the NSF scattering is featureless (Fig. 1d,e). These data indicate that the excitations at 10 and 3 meV near $\mathbf{Q} = (1/2, 1/2)$ are entirely magnetic in origin and without any lattice contribution to the scattering. On warming to 30 K (Fig. 1f), the intensities of the 10 meV excitations decrease, and are consistent with a prototypical neutron spin resonance mode[14]. Figure 1g shows that SF scattering for the neutron polarization direction parallel to the **Q**-direction is about twice as large as for those perpendicular to it. This indicates that the resonance is due to isotropic paramagnetic scattering[23] and is consistent with the mode being a singlet-to-triplet excitation associated with electron pairing[24].

To determine the energy dependence of the dynamic spin susceptibility $\chi''(Q, \omega)$, we measure energy scans at the AF wave vector $\mathbf{Q} = (1.5, -0.5)$ and background $(1.64, -0.36)$ positions above and below T_c. Figure 2a,b shows the raw data for SF and NSF scattering, respectively. The SF magnetic data in Fig. 2a are dominated by the wave-vector-independent Pr^{3+} crystalline electric field (CEF) level near 18 meV (refs 15,25), whereas the weak peak near 16 meV in the NSF scattering is due to imperfect neutron polarization and nonmagnetic phonon scattering. Figure 2c shows $\chi''(Q, \omega)$ at $\mathbf{Q} = (1.5, -0.5)$ in absolute units, obtained by subtracting the background scattering, including the Pr^{3+} CEF, including low-energy data (see Supplementary Information), correcting for the Bose population factor, and normalizing to acoustic phonons[26]. The outcome reveals two broad peaks at $\sim$2 and 10.5 meV that are enhanced below T_c. Solid lines in this plot are simple guides to the eye obtained by fitting two Gaussians to identify the mode energies. To determine the T_c evolution of the resonance and 2 meV excitations, we plot $\chi''(Q, \omega)$ in Fig. 2d for both the $T_c = 24$ and 21 K PLCCO (refs 11,14,15 and Supplementary Information). We find that the effect of decreasing T_c from the 24 to 21 K in PLCCO through the annealing process is to enhance the 2 meV mode and reduce the intensity of the neutron spin resonance near 9 meV (Fig. 2d).

We now turn to STM measurements that can directly probe the superconducting state and its spatial distribution. PLCCO samples were cleaved in UHV and directly inserted into the STM head held at 5 K. Data from five samples and tips (three 24 K PLCCO samples and two 21 K PLCCO samples) are included in this paper. We studied multiple spots within each sample, which also contributes to our robust set of statistics. The lack of a periodic lattice on the surface of PLCCO makes other methods of tip and sample characterization crucial to ensure the reliability of the data. Tips were characterized on the prototypical superconductor $Bi_2Sr_2CaCu_2O_8$. Scanning electron microscopy (SEM) studies reveal large micrometre-sized flat regions, which were accessed using our ability to move to different regions with the coarse motion mechanism of the STM (more details on tip and sample characterization are described in the Supplementary Information).

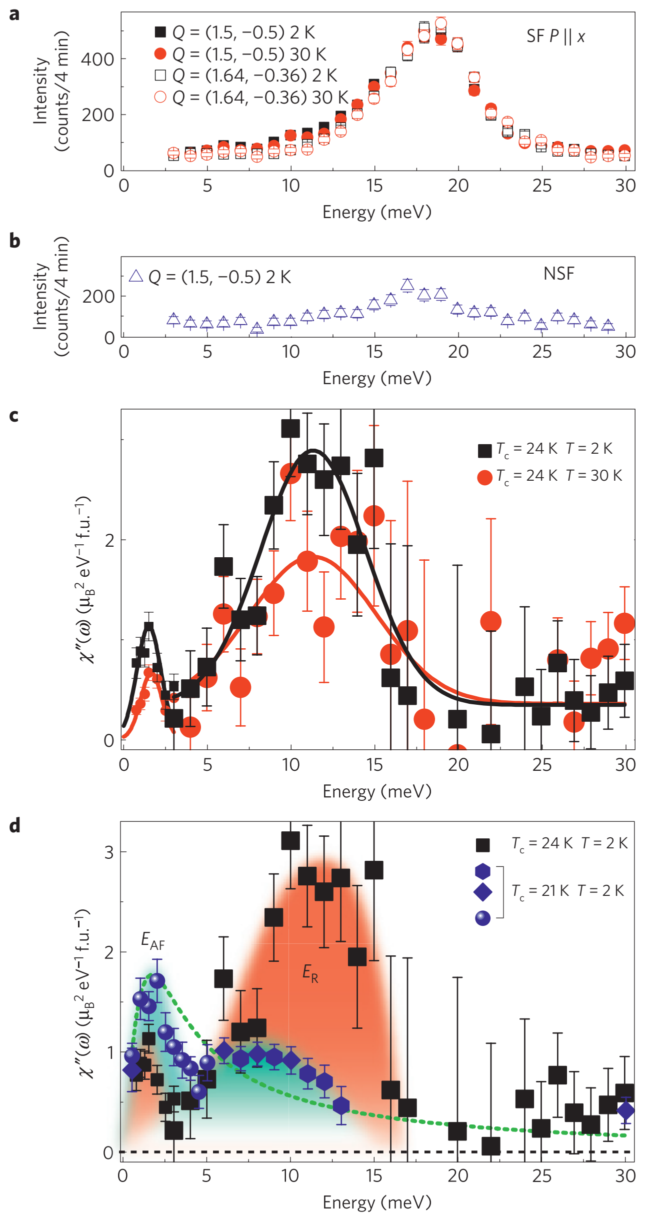

Figure 2 | Energy dependence of SF and NSF scattering at $\mathbf{Q} = (1.5, -0.5, 0)$ rlu for the 24 K PLCCO and $\chi''(\omega)$ in absolute units for the 21 and 24 K samples. **a**, Energy scans at the signal $\mathbf{Q} = (1.5, -0.5, 0)$ and background $\mathbf{Q} = (1.64, -0.36, 0)$ positions at 2 K and 30 K in the SF channel, the **Q**-independent 18 meV peak originates from the CEF excitation of Pr^{3+} (ref. 25). **b**, Energy scans at $\mathbf{Q} = (1.5, -0.5, 0)$ in the NSF channel. **c**, The combined and normalized low-energy $\chi''(\omega)$ above and below T_c for the 24 K PLCCO in absolute units. The black and red solid lines are guides-to-the-eye based on a weighted Gaussian fit for 2 K and 30 K data, respectively. **d**, Comparison of the $\chi''(\omega)$ for the 24 K and 21 K PLCCO at 2 K. The data for the 21 K PLCCO are from Figs 5a and 6a–c of ref. 13 (blue circles) normalized to the data in absolute units from ref. 15 (diamond shaped squares). The hexagons indicate data from ref. 11 normalized with data from refs 13,15. The green dashed line shows an attempted fit using a modified Lorentzian, which clearly cannot fit the data.

Compared with the $T_c = 24$ K PLCCO, the 21 K samples have smaller superconducting gaps (5.5 ± 0.5 meV versus 7.7 ± 1.2 meV

NATURE PHYSICS DOI: 10.1038/NPHYS2006

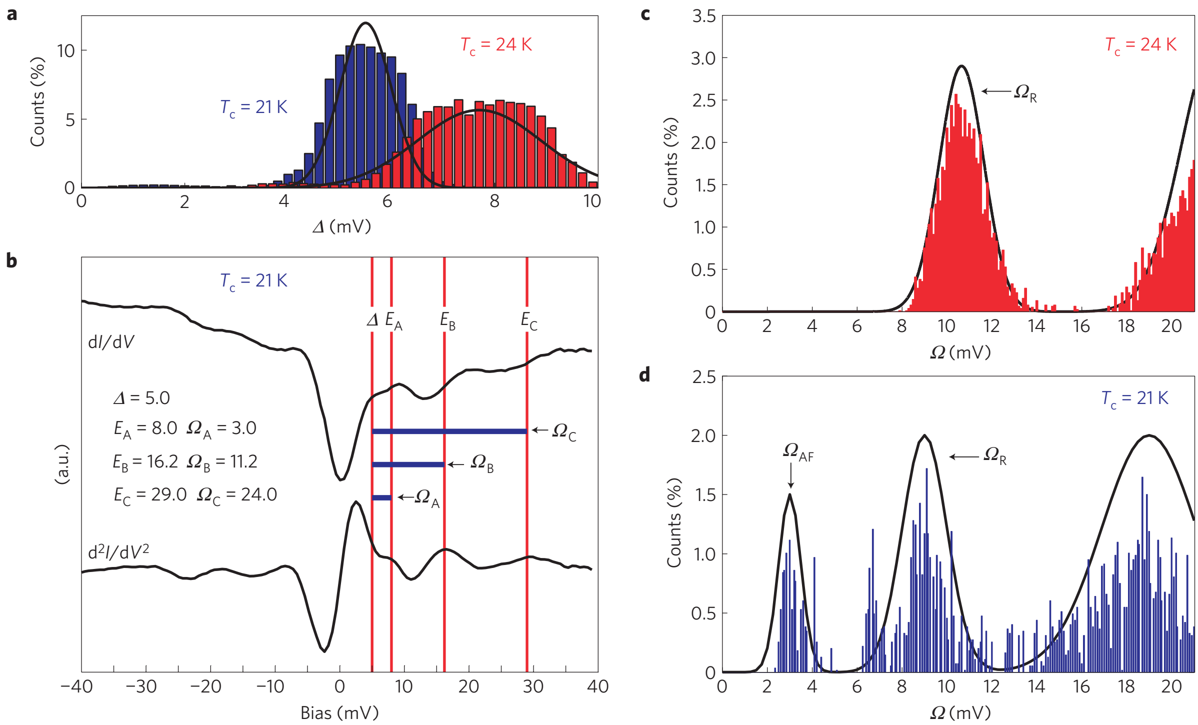

Figure 3 | Comparison of the tunnelling spectra of the 21 and 24 K samples. Our STS measurements were performed on the same instrument as described previously[18]. **a**, Histogram showing the distribution of the superconducting gaps for the 21 K and 24 K PLCCO samples. **b**, Single dI/dV spectrum of the 21 K PLCCO and its derivative (d^2I/dV^2) offset below, demonstrating the existence of the superconducting gap and the three modes in the same spectrum. The derivative was smoothed (using nearest-neighbour averaging) and multiplied by a simple factor. The spectrum was obtained with a junction resistance of 16.5 MΩ. The energies of the local gap (Δ) and the three features (E_A, E_B, and E_C) from which the corresponding mode energies are calculated are shown on the figure. **c**,**d**, Comparison of the mode statistics for the 21 K and 24 K samples. A Gaussian fit to the data is shown as a guide to the eye. The 21 K samples shows three modes, $\Omega_{AF} = 3.0 \pm 0.3$ meV, $\Omega_R = 9.2 \pm 0.85$ meV, and a third mode at 19.2 ± 2.1 meV. Note that Ω_A and Ω_B in **b** are now called Ω_{AF} and Ω_R. The 24 K data shows the primary mode ~10.5 meV and part of the second mode ~21 meV. The 21 K Ω_R modes are shifted with respect to the 24 K sample. The 3 meV, Ω_{AF} mode, which is clearly visible in the 21 K data, is rarely observed in the 24 K data and therefore does not have a presence in the histogram.

for the 24 K samples, Fig. 3a) that disappear just above the bulk T_c and below T_N (see Supplementary Fig. SI4). We note that the smaller value of the standard deviation for the statistical average for the 21 K sample is possibly the result of a smaller statistical pool for the 21 K PLCCO than for the 24 K PLCCO, thus making the distribution narrower. However, it is clear that the entire gap histogram is shifted to lower energies for the 21 K sample, resulting in a lower average gap. In general, the 21 K gaps have muted coherence peaks (Figs 3b and 4d) compared to those of the 24 K samples[18]. The heights and widths of the coherence peaks are a measure of the scattering rate (Γ), which contains a temperature-dependent contribution from phonons and electronic excitations, as well as a temperature-independent contribution from impurity scattering (Γ_{imp}) (refs 27,28). The smaller heights (larger widths) of the coherence peaks at the same measurement temperatures as 24 K samples indicate a larger impurity Γ_{imp} in the 21 K PLCCO. As the two samples have nominally identical Ce concentrations, the additional disorder is probably due to the in-plane defects, which is consistent with more in-plane Cu vacancies in the lower T_c sample[10].

In the 21 K samples, outside the gap (Δ) we observe three distinct satellite features, labelled E_A, E_B and E_C in Fig. 3b, that originate from the coupling of electrons to collective excitations (bosonic modes, which can be either spin excitations[18] or phonons[29]) in the sample. Our first task is to obtain the energy of these bosonic modes from the STS spectra. In a superconductor, a bosonic excitation at energy Ω results in a feature at energy (E), offset by the gap in the tunnelling spectroscopy[18,29]. The local bosonic mode energy can therefore be determined from the STS spectrum by subtracting the local gap energy scale, that is, $\Omega = E - \Delta$. The energy E is best determined (see Supplementary Information) by locating the position of the maxima/minima in the second derivative of the tunnel current, d^2I/dV^2, above and below the Fermi energy respectively (Fig. 3b). We first consider the higher energy features, labelled E_B and E_C in Fig. 3b.

Statistics for Ω_B and Ω_C (Fig. 3d) reveal that the average energies are 9.2 ± 0.85 meV (we henceforth term this mode Ω_R) and 19.2 ± 2.1 meV. Standard deviations were calculated from the Gaussian fit to the histograms, as shown in Fig. 3d. These energies are reminiscent of the modes found in our earlier STS studies of 24 K PLCCO samples (~10.5 and 21 meV; ref. 18), where the neutron spin resonance is found to occur at ~11 meV (ref. 14; Fig. 2c). The correspondence in energy, combined with the absence of a peak in the phonon density of states at ~11 meV (Fig. 2b), had suggested a common origin for the STS and neutron modes, with the 21 meV feature possibly arising from a second harmonic process[18]. We note that there are phonon modes at energies above 15 meV (ref. 18) that could also contribute to the spectral intensity in STM spectra. This may explain why in some cases the intensity of Ω_C is comparable to that of Ω_B. STM data alone cannot distinguish between these possibilities for the higher energy mode; however our unique combined STM and neutron studies suggest a magnetic origin. Most importantly, this does not affect any conclusions about Ω_B. In the 21 K PLCCO, the same neutron spin resonance is found to shift to a lower energy of ~9.3 meV in accordance with the lower T_c (ref. 11;

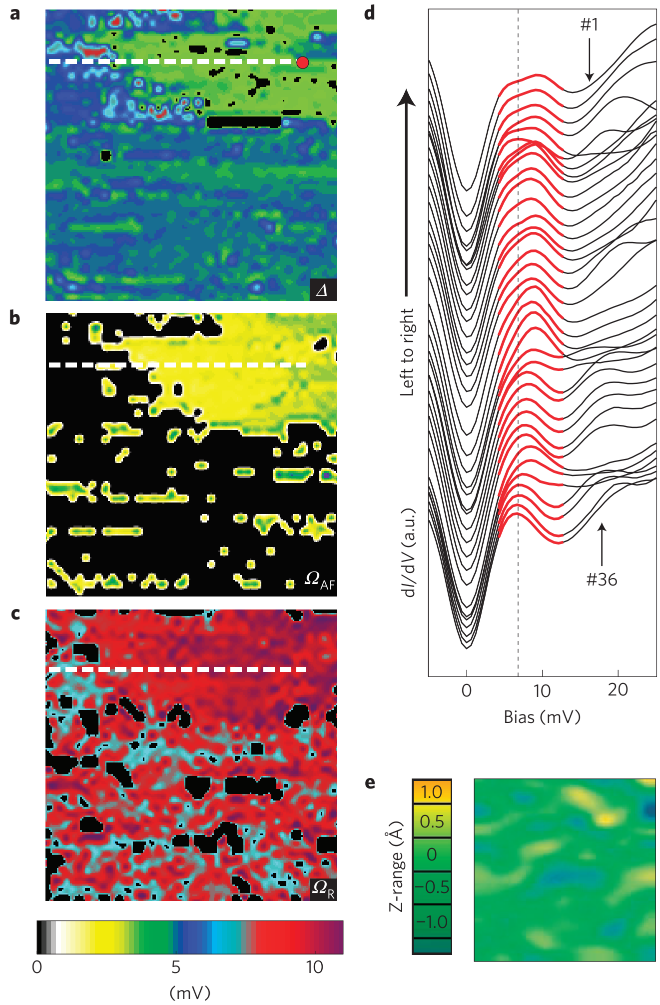

Figure 4 | Spatial variation of gap and Bosonic modes. 90 Å maps of the same area of the 21 K sample showing (**a**) Δ, (**b**) Ω_{AF}, and (**c**) Ω_R. All the maps have the same colour scale, which is shown at the bottom. The dashed line shows the position of the 70 Å linecut in **d**. **d**, The linecut shows the transition from a spectrum showing a clear low-energy mode Ω_{AF} (labelled #1, shown as a red dot on the Δ map) to a spectrum (labelled #36) at the end of the linecut, where the coherence peak and Ω_{AF} seem to have merged into one entity. The dotted line traces the low-energy mode as it evolves. The energy range of interest is highlighted in red. The spectra were obtained at 2 Å intervals and have been offset for clarity. All spectra were obtained with a junction resistance of 16.5 MΩ. **e**, Topography in the same region as the maps.

Fig. 2c). The corresponding downward energy shift of the STS mode (Fig. 3c,d) provides strong support for its identification with the spin resonance. Consistent with this picture, the broad higher energy feature is also shifted to lower energies. We note that similar to the 24 K sample[18], the intensity of the spin resonance mode in the 21 K data shows spatial variations. But whereas the mode is observed in ~85% of spectra in the 24 K samples, the 21 K samples show more areas where the intensity of the mode is suppressed such that it is observed in only ~63% of the spectra. This is consistent with the fact that the 21 K sample has a weaker superconducting heat capacity anomaly[11].

Having identified the 9.2 meV mode with the neutron spin resonance, we turn to the lower energy feature, labelled E_A in Fig. 3b. From the mode statistics (Fig. 3d), we obtain an average energy of 3.0 ± 0.3 meV; we name this new mode Ω_{AF}. As there is no peak in the phonon density of states at these energies (Fig. 2b), we look at electronic excitations to explain its origin. As-grown PLCCO exhibits three-dimensional AF order below $T_N \approx 200$ K (ref. 13). Neutron scattering data show that on annealing to remove oxygen and obtain the 21 K sample, T_N reduces to ~40 K and there is a drastic renormalization of the spin dynamics with a peak in the low-temperature local spin susceptibility ($\chi''(\omega)$) appearing near ~2 meV (refs 10–15). This low-energy mode is reminiscent of the overdamped excitation observed to emerge in hole-doped $YBa_2Cu_3O_{6.35}$ close to the AF phase boundary[30] and is a potential candidate for Ω_{AF}. In the neutron data, the 2 meV neutron peak in the 21 K sample is rapidly suppressed in the 24 K sample(refs 11,14,15). This is in stark contrast to the spin resonance mode (~10 meV), for which the energy and spectral weight are enhanced on tuning toward higher T_c (Fig. 2c). In remarkable agreement with the neutron scattering data, we find that Ω_{AF} is more prominent in the 21 K sample compared to the 24 K sample, for which this mode is only rarely observed; and quite opposite to the behaviour of Ω_R. The correspondence in energy and doping dependence make it highly credible that Ω_{AF} and Ω_R have a magnetic origin, similar to the neutron modes with the same energy.

Keeping in mind that Ω_{AF} is a signature of local AF order, we construct spatial maps for Ω_{AF} and Ω_R (Fig. 4b,c) in the 21 K sample. Comparing the maps we find that there are nanometre-sized regions where Ω_{AF} and Ω_R are both present. These areas are not macroscopically segregated but are rather fully embedded within the superconducting regions. The data clearly show that AF order and superconductivity coexist at nanometre length scales. The question remains whether the coexistence is ubiquitous or confined to nanometre-sized patches. From the neutron studies, we know that the 21 K sample has macroscopic AF phase coherence associated with static long-range AF order[12]. Therefore, it seems likely that Ω_{AF} should also exist in extended, contiguous regions of the sample. There are two possible explanations for the seemingly contrary nature of Ω_{AF} in the STS data. First, similar to Ω_R, the varying intensity of the mode makes it difficult to discern in some regions. However, there is a second, more compelling explanation. As seen in the histogram (Fig. 3d), the mode energy varies, reflecting the spatial inhomogeneity of the AF order. As the mode lies close to the gap edge, a small decrease in the mode energy pushes it toward the gap edge, merging it with the coherence peak. This is clearly seen in the line-cut (Fig. 4d) as we go from a coexisting region (spectrum 1) to the area where the mode is indistinguishable from the coherence peak (spectrum 36). A closer analysis of the STS data thus indicates that the mode might well be widespread but simply difficult to see once it merges with the coherence peak, implying that the STM analysis probably overestimates the energy of Ω_{AF}. As the neutron data represent an average over all regions, this accounts for the smaller neutron mode energy.

This scenario is further supported by the gap map (Fig. 4a), which shows clear spatial correlation with the Ω_{AF} mode map. Comparing the two, we find that the regions with a prominent Ω_{AF} mode are found with smaller superconducting gaps (and minimal coherence peaks). The larger gap regions are associated with an underlying smaller and weaker Ω_{AF}, making it hard to distinguish from the coherence peaks. We therefore conclude that the raw STS data most likely underestimates the size of the coexisting region. This, in conjunction with the neutron data, illustrates a picture of a long-range ordered AF phase in the 21 K compound that weakens on further annealing into short-ranged, local AF order and correspondingly higher T_c values, as seen in the 24 K sample. Finally, given that one does not expect phonons to change for the 21 and 24 K samples, our results (Figs 2c and 3c,d) represent the most compelling evidence that spin excitations are intimately associated with the tunnelling electronic bosonic modes observed by STS.

Received 4 July 2010; accepted 19 April 2011; published online 22 May 2011

References

1. Lee, P. A., Nagaosa, N. & Wen, X. G. Doping a Mott insulator: Physics of high-temperature superconductivity. *Rev. Mod. Phys.* **78,** 17–85 (2006).
2. Armitage, N. P., Fournier, P. & Greene, R. L. Progress and perspectives on the electron-doped cuprates. *Rev. Mod. Phys.* **82,** 2421–2487 (2010).
3. Capone, M. & Kotliar, G. Competition between d-wave superconductivity and antiferromagnetism in the two-dimensional Hubbard model. *Phys. Rev. B* **74,** 054513 (2006).
4. Demler, E., Hanke, W. & Zhang, S-C. SO(5) theory of antiferromagnetism and superconductivity. *Rev. Mod. Phys.* **76,** 909–974 (2004).
5. Weber, C., Haule, K. & Kotliar, G. Strength of correlations in electron and hole doped cuprates. *Nature Phys.* **6,** 574–578 (2010).
6. Tranquada, J. M., Sternlieb, B. J., Axe, J. D., Nakamura, Y. & Uchida, S. Evidence for stripe correlations of spins and holes in copper oxide superconductors. *Nature* **375,** 561–563 (1995).
7. Kivelson, S. A. *et al.* How to detect fluctuating stripes in the high-temperature superconductors. *Rev. Mod. Phys.* **75,** 1201–1241 (2003).
8. Pintschovius, L. & Reichardt, W. in *Physical Properties of High Temperature Superconductors,* Vol. IV (ed. Ginsberg, D. M.) 295 (World Scientific, 1994).
9. Fujita, M. *et al.* Magnetic and superconducting phase diagram of electron-doped $Pr_{1-x}LaCe_xCuO_4$. *Phys. Rev. B* **67,** 014514 (2003).
10. Kang, H. J. *et al.* Microscopic annealing process and its impact on superconductivity in T'-structure electron-doped copper oxides. *Nature Mater.* **6,** 224–229 (2007).
11. Li, S. L. Impact of oxygen annealing on the heat capacity and magnetic resonance of superconducting $Pr_{0.88}LaCe_{0.12}CuO_{4-\delta}$. *Phys. Rev. B* **78,** 014520 (2008).
12. Dai, P. *et al.* Electronic inhomogeneity and competing phases in electron-doped superconducting $Pr_{0.88}LaCe_{0.12}CuO_{4-\delta}$. *Phys. Rev. B* **71,** 100502(R) (2005).
13. Wilson, S. D. *et al.* Evolution of low-energy spin dynamics in the electron-doped high-transition temperature superconductor $Pr_{0.88}LaCe_{0.12}CuO_{4-\delta}$. *Phys. Rev. B* **74,** 144514 (2006).
14. Wilson, S. D. *et al.* Resonance in the electron-doped high-transition-temperature superconductor $Pr_{0.88}LaCe_{0.12}CuO_{4-\delta}$. *Nature* **442,** 59–62 (2006).
15. Wilson, S. D. *et al.* High-energy spin excitations in the electron-doped superconductor $Pr_{0.88}LaCe_{0.12}CuO_{4-\delta}$ with $T_c = 21$ K. *Phys. Rev. Lett* **96,** 157001 (2006).
16. Dagan, Y., Qazilbash, M. M., Hill, C. P., Kulkarni, V. N. & Greene, R. L. Evidence for a quantum phase transition in $Pr_{2-x}Ce_xCuO_{4-\delta}$ from transport measurements. *Phys. Rev. Lett.* **92,** 167001 (2004).
17. Motoyama, E. M. *et al.* Spin correlations in the electron-doped high-transition-temperature superconductor $Nd_{2-x}Ce_xCuO_4$. *Nature* **445,** 186–189 (2007).
18. Niestemski, F. C. *et al.* A distinct bosonic mode in an electron-doped high-transition-temperature superconductor. *Nature* **450,** 1058–1061 (2007).
19. Zhao, G. M. Fine structure in the tunneling spectra of electron-doped cuprates: No coupling to the magnetic resonance mode. *Phys. Rev. Lett* **103,** 236403 (2009).
20. Bardeen, J., Cooper, L. N. & Schrieffer, J. R. Theory of superconductivity. *Phys. Rev.* **108,** 1175–1204 (1957).
21. McMillan, W. L. & Rowell, J. M. Lead phonon spectrum calculated from superconducting density of states. *Phys. Rev. Lett.* **14,** 108–112 (1965).
22. Maier, T. A., Poilblanc, D. & Scalapino, D. J. Dynamics of the pairing interaction in the Hubbard and $t-J$ models of high-temperature superconductors. *Phys. Rev. Lett* **100,** 237001 (2008).
23. Moon, R. M., Riste, T. & Koehler, W. C. Polarization analysis of thermal-neutron scattering. *Phys. Rev.* **181,** 920–931 (1969).
24. Eschrig, M. The effect of collective spin-1 excitations on electronic spectra in high-T_c superconductors. *Adv. Phys.* **55,** 47–183 (2006).
25. Boothroyd, A. T., Doyle, S. M., Paul, D. M. K. & Osborn, R. Crystal-field excitations in Nd_2CuO_4, Pr_2CuO_4, and related n-type superconductors. *Phys. Rev. B* **45,** 10075–10086 (1992).
26. Kruger, F. *et al.* Magnetic fluctuations in n-type high-T_c superconductors reveal breakdown of fermiology: Experiments and Fermi-liquid/RPA calculations. *Phys. Rev. B* **76,** 094506 (2007).
27. Pasupathy, A. N. *et al.* Electronic origin of the inhomogeneous pairing interaction in the high-T $_c$ superconductor $Bi_2Sr_2CaCu_2O_{8+d}$. *Science* **320,** 196–201 (2008).
28. Alldredge, J. W. *et al.* Evolution of the electronic excitation spectrum with strongly diminishing hole density in superconducting $Bi_2Sr_2CaCu_2O_{8+\delta}$. *Nature Phys.* **4,** 319–326 (2008).
29. Lee, J. *et al.* Interplay of electron–lattice interactions and superconductivity in $Bi_2Sr_2CaCu_2O_{8+\delta}$. *Nature* **442,** 546–550 (2006).
30. Stock, C. *et al.* Central mode and spin confinement near the boundary of the superconducting phase in $YBa_2Cu_3O_{6.353}$ ($T_c = 18$ K). *Phys. Rev. B* **73,** 100504(R) (2006).

Acknowledgements

The neutron scattering work at UT/ORNL is supported by the US NSF-OISE-0968226, and by the US DOE, Division of Scientific User Facilities (P.D.). Work at BC is supported by US NSF-CAREER-0645299 (V.M.) and DOE DE-SC0002554 (Z.W.). The single crystal PLCCO growth effort at UT is supported by US DOE BES under Grant No. DE-FG02-05ER46202 (P.D.). Work at IOP is supported by the Chinese Academy of Sciences, the Ministry of Science and Technology of China (973 Project nos. 2010CB833102 and 2010CB923002). J.Z. is supported by a fellowship from Miller Institute of Basic Research in Science at Berkeley.

Author contributions

P.D. and V.M. planned the neutron and STM experiments, respectively. J.Z., S.L., P.S., A.H., H.J.K., S.D.W. and P.D. carried out neutron scattering measurements and data analysis. F.C.N., S.K. and V.M. performed STM/STS measurements. The samples were grown by J.Z. and S.L. The paper was written by P.D., V.M. and Z.W. with input from J.Z., S.D.W., and F.C.N. All coauthors provided comments on the paper.

Additional information

The authors declare no competing financial interests. Supplementary information accompanies this paper on www.nature.com/naturephysics. Reprints and permissions information is available online at http://www.nature.com/reprints. Correspondence and requests for materials should be addressed to P.D. or V.M.